PCCP

ROYAL SOCIETY OF CHEMISTRY

PAPER

View Article Online
View Journal | View Issue

Cite this: *Phys. Chem. Chem. Phys.*, 2023, **25**, 25344

Momentum matching induced giant magnetoresistance in two-dimensional magnetic tunnel junctions

Yaohua Qiu,[a] Chun-Sheng Liu,[b] Xingqiang Shi,[c] Xiaohong Zheng *[a] and Lei Zhang *[de]

Received 3rd July 2023,
Accepted 21st August 2023

DOI: 10.1039/d3cp03121g

rsc.li/pccp

Giant magnetoresistance was first experimentally discovered in three-dimensional magnetic tunnel junctions (MTJs) in the late 1980s and is of great importance in nonvolatile memory applications. How to achieve a magnetoresistance as large as possible is always a central task in the study of MTJs. However, it is normally only of the order of magnitude of tens of percent in traditional MTJs. The ideal situation is the metal–insulator transition together with the magnetization reversal of one magnetic lead. In this work, we will show that this can be achieved using a two-dimensional ferromagnetic zigzag SiC nanoribbon junction based on quantum transport calculations performed with a combination of density functional theory and non-equilibrium Green's function. Specifically, with the magnetization configuration switching of the two leads from parallel to anti-parallel, the junction will change abruptly from a conducting state to an insulating state, although the two leads are always metallic, with both spin up and spin down channels crossing the Fermi level simultaneously. Extensive analysis indicates that the insulating state in the anti-parallel magnetic configuration originates not from any present mechanisms that cause full suppression of electron transmission but from momentum direction mismatching. This finding suggests a fantastic mechanism for achieving magnetoresistance or electrical switching in nanoscale devices by manipulating band dispersion.

1. Introduction

The discovery of a giant magnetoresistance (GMR) effect in magnetic tunnel junctions (MTJs) by Fert and Grünberg *et al.* in the late 1980s started a revolution of data storage technology in computer science.[1,2] Resulting from it, the data storage density was substantially increased by tens of times and it rapidly became the standard memory technology in digital products such as computers and digital cameras. Starting from this discovery, a new subject called spintronics appeared and the spin degree of freedom of electrons as a carrier of information started to attract the intensive attention of researchers.[3–12]

Traditional three dimensional MTJs are composed of an insulator sandwiched between two ferromagnetic leads.[13] When the magnetizations of the two leads are parallel, one spin channel will be in a highly conducting state and the other spin channel will be in a lowly conducting state. As a two-channel parallel resistor model, it will result in a low resistance state. In contrast, when the magnetizations of the two leads are anti-parallel, both channels will be largely blocked and thus a high resistance state arises. However, the magnetoresistance is generally very low, typically on the order of tens of percent.[1,2] Thus, it is always a central task to achieve magnetoresistance as large as possible. Theoretically, the ideal situation is the metal–insulator transition together with the magnetization configuration switching between parallel and anti-parallel. In traditional three dimensional MTJs, this is hardly achievable unless both magnetic leads are half-metallic, with only one spin channel crossing the Fermi level in the band structure of each lead.

Together with the rise of two-dimensional (2D) materials starting from the discovery of graphene,[14–17] 2D magnetic materials with intrinsic magnetism are successively proposed theoretically or synthesized experimentally, such as $Gr_2Ge_2Fe_6$, CrI_3, VSe_2, $CrGeTe_3$, Fe_3GeTe_2, NiPS, CoH_2, $CrBr_3$, *etc.*[18–27] More

[a] College of Information Science and Technology, Nanjing Forestry University, Nanjing 210037, China. E-mail: xhzheng@njfu.edu.cn
[b] College of Electronic and Optical Engineering, Nanjing University of Posts and Telecommunications, Nanjing 210023, China
[c] College of Physics Science and Technology, Hebei University, Baoding 071002, China
[d] State Key Laboratory of Quantum Optics and Quantum Optics Devices, Institute of Laser Spectroscopy, Shanxi University, Taiyuan 030006, China. E-mail: zhanglei@sxu.edu.cn
[e] Collaborative Innovation Center of Extreme Optics, Shanxi University, Taiyuan 030006, China

interestingly, some 2D materials, such as graphene[28] and 2D SiC,[29] are intrinsically nonmagnetic but become magnetic when they are cut into one-dimensional nanoribbons with zigzag edges. The spatially separated edge states cause edge magnetism which may be in either anti-ferromagnetic or ferromagnetic coupling between the two edges. The availability of 2D magnetic materials and magnetic nanostructures greatly enhances the development of spintronics in the field of low dimensional systems. Specifically, giant magnetoresistance devices have also been proposed based on zigzag graphene nanoribbons (ZGNRs).[30–35] Interestingly, several mechanisms based on the appearance/disappearance of states at the Fermi level,[30] spin matching/mismatching[31] or orbital symmetry matching/mismatching[32] have been proposed to achieve conducting–insulating transition with the switching of the magnetic field in the MTJs.

Specifically, magnetoresistance is related to different transmission probabilities between the parallel and anti-parallel magnetization configurations. Whether an electron can tunnel through the barrier from one lead to the other lead depends on many factors. First of all, both the left and right leads should be conducting. In terms of electronic structure, for an electron with energy E to transmit, the density of states (DOS) in both leads should be nonzero at this energy E. Muñoz-Rojas's scheme uses the metallic ferromagnetic state and the insulating antiferromagnetic state of ZGNRs as the tunnel barrier to realize GMR. The switching of the states is realized by applying or not applying a magnetic field to the central ZGNR.[30] Secondly, the spin channels of the two leads should match. Even if the DOS is not zero, if the spin channel does not match, the electrons cannot tunnel from one lead to the other. With this mechanism, the conducting state and the insulating state can be achieved by using half-metals as the two leads and a magnetic field to tune the spin polarity of the half-metallicity.[31,36] In this situation, if the two leads are parallel in magnetizations, electrons can transmit. In contrast, if the two leads are have anti-parallel magnetizations, electrons cannot transmit due to the spin mismatch in systems without spin–orbit interactions. Thirdly, the orbital symmetries of the two leads should not be orthogonal to each other. If it is odd symmetry in one lead and even symmetry in the other lead, the electrons cannot transmit due to the orbital orthogonality in the two leads.[32,37] To obtain an insulating state together with the magnetization reversal, at least one of the above conditions should be satisfied.

In this work, by adopting a ferromagnetic zigzag SiC nanoribbon (ZSiCNR) for constructing a MTJ, we will show that the junction will undergo a conducting–insulating transition together with the magnetization configuration switching between the two leads, leading to giant magnetoresistance. It is quite unusual considering the facts of both leads being metals with both spin channels crossing the Fermi level in the band structure and the orbital nonorthogonality between the two leads. Extensive analysis indicates that it originates from none of the above three mechanisms, but from a new one based on momentum matching or mismatching.

2. Simulation model and calculation details

The two-probe MTJ in study is constructed with an 8-ZSiCNR which contains 8 zigzag SiC chains along the x direction in width. The junction is divided into three parts: the left lead (left), the right lead (right), and the central region (central). Although there is some arbitrariness in choosing the central region in an infinite nanoribbon, we still have to make sure that the central region should be long enough so that the potential in the central region will saturate to that of the bulk leads at its boundaries. In this work, 16 unit cells are chosen as the central region, with the central eight unit cells for denoting the magnetic configuration shown in Fig. 1(a) and its two ends are periodically repeated to infinity along the z axis on both sides as the leads (not shown). The transport direction of the junction is along the z-axis. The size of the central region is $56.0 \times 12.5 \times 49.6$ Å, which is large enough to avoid the interaction from its periodic images in the xy plane. The parallel ("P") magnetization configuration is obtained by setting the initial edge atomic magnetic moments in the whole central region to be up while the anti-parallel ("AP") magnetization configuration is obtained by setting the initial edge atomic magnetic moments of the left half to up and those of the right half to down. In experiment, we may apply parallel or antiparallel magnetic fields to the two leads and not to the central region. Due to the proximity effect and the strong FM coupling between the edge Si or C atoms at the same edge, the neighbor edge atoms will be polarized with the same magnetization direction. The spontaneous extension of the magnetization relaxation from the two leads to the device center will automatically produce a uniform magnetization in the P case and a magnetic boundary at the device center in the AP case.

First-principles calculations are performed using the Nanodcal package which combines density functional theory and non-equilibrium Green's function techniques for the quantum transport study.[38,39] The wave functions are expanded by linear combinations of atomic orbitals (LCAOs) in the form of double zeta polarized basis (DZP). The atomic cores are described using norm-conserving pseudopotentials and the exchange–correlation potential is treated at the level of the generalized gradient approximation (GGA) in the form of Perdew–Burke–Ernzerhof (PBE).[40] The real space mesh grid is determined by a cutoff energy of 50 Ry. For the lead self-consistency and electron transport calculations of this MTJ, the k-grids of the reciprocal space are set to $1 \times 1 \times 100$ and $1 \times 1 \times 1$, respectively. The density matrix and the Hamiltonian convergence criterion are both set to 1×10^{-4} a.u. The force convergence criterion is set as 0.04 eV Å^{-1} for geometry relaxation.

The spin-resolved conductance is calculated by

$$G_\sigma = \frac{e^2}{h} T_\sigma(E_F) \quad (1)$$

where e is the electron charge, h is the Planck constant, and $T_\sigma(E_F)$ is the spin-resolved transmission coefficient with spin $\sigma(\sigma = \uparrow, \downarrow)$ at the Fermi level E_F. $T_\sigma(E)$ is calculated by

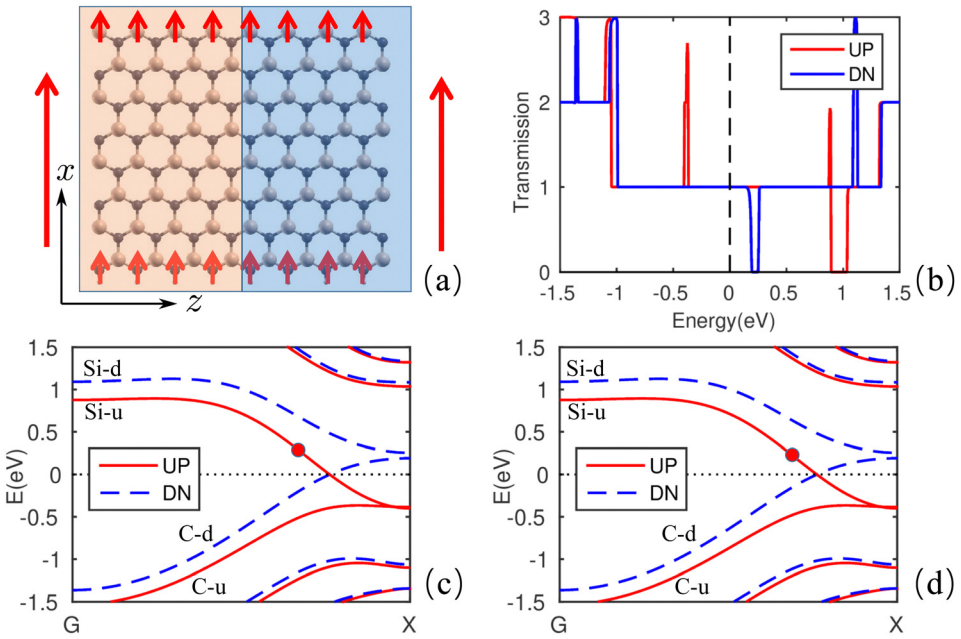

Fig. 1 (a) The central region of the device S1 with a parallel magnetic configuration ("S1-P"). (b) The equilibrium transmission function. (c) The band structure of the left lead. (d) The band structure of the right lead. The red dots mark two spin-matching (spin up) bands crossing the Fermi level in the two leads.

$$T_\sigma(E) = Tr[\Gamma_L(E)G^R(E)\Gamma_R(E)G^A(E)]_\sigma \quad (2)$$

where $G^{R(A)}$ is the retarded (advanced) Green's function of the central region and $\Gamma_{L(R)}$ is the linewidth function of the left (right) lead which describes the coupling between the lead and the central scattering region.

3. Results and discussion

Although silicon prefers sp^3 instead of sp^2 hybridization, thus 2D silicon materials cannot be constructed, it is possible to form a layered structure by mixing C and Si with sp^2 hybridization. SiC nanotubes[41,42] and 2D SiC sheets[29] are such typical examples and both have been successfully synthesized. Unlike carbon nanotubes which may be metallic or semiconducting depending on the chirality, SiC nanotubes and 2D SiC materials are all semiconductors. Just like carbon nanotubes and graphene that can be cut into 2D nanoribbons, SiC nanotubes and 2D SiC sheets can also be cut into nanoribbons. Very interestingly, SiC nanoribbons with zigzag edges are magnetic, with edge states and edge magnetism localized on the two edges.[43–46] More interestingly, the ground state is an antiferromagnetic (AFM) one with a ferromagnetic (FM) order in one edge and an antiferromagnetic order between the two edges and it is intrinsically half-metallic. However, this half-metallicity is basically useless since its energy is only very slightly less than or even almost equal to that of the ferromagnetic state.[44] Thus, the antiferromagnetic state cannot be stabilized. Nevertheless, the ferromagnetic state can be fixed by applying a magnetic field or by putting the sample on a magnetic substrate. This enables the convenience of studying the magnetoresistance effect which needs both leads to be ferromagnetic and the switching between parallel and antiparallel can be accomplished by applying magnetic fields with identical or opposite directions. Thus, our study in the following will focus on the ferromagnetic state of zig-zag SiC nanoribbons.

The band structure of the 8-SiCNR in the ferromagnetic state is shown in Fig. 1(c). It is seen that there are one spin up band and one spin down band crossing the Fermi level, and thus, it is a metal in terms of band theory. Since the transport properties of materials are determined by the bands around the Fermi level, we plot the wave functions of the four bands at $k = 0.35\frac{2\pi}{a}$ (a is the lattice constant of the primitive cell along the periodic direction) to see the spatial distribution of these states, as shown in Fig. 2. It is seen that the two bands starting from the Γ point above the Fermi level and going down from left to right are localized on the Si-edge. In contrast, the two bands starting from the Γ point below the Fermi level and going up from left to right are localized on the C-edge. Here, the Si-edge or C-edge mean the edge terminated with Si or C atoms apart from the passivating H atoms. The four bands closest to the Fermi level are thus marked with 'Si-d', 'Si-u', 'C-d' and 'C-u', denoting the spin down(up) band localized on the Si(C)-edge, with 'd' and 'u' denoting 'spin down' and 'spin up', respectively. From the atomic magnetic moments shown in Fig. 2(d), the magnetism is extremely localized at the edges, with maxima of $0.276\mu_B$ at the Si atom and $0.254\mu_B$ at the C atom, decaying rapidly away from them to the center. Since the magnetic moments of most internal atoms are close to zero, the magnetic coupling between the two edges is weak and the difference between the AFM and FM configurations is negligibly small in this system.[44]

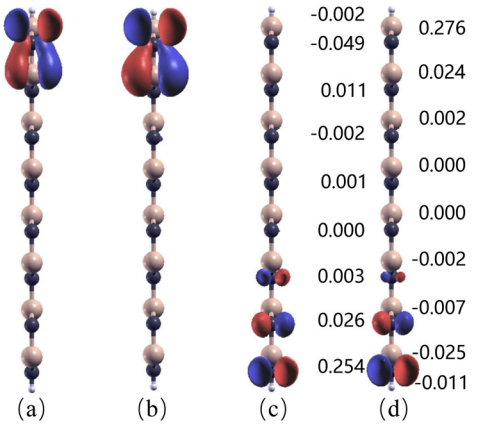

Fig. 2 The state at $k = 0.35\left(\frac{2\pi}{a}\right)$ for (a) the Si-u band, (b) the Si-d band, (c) the C-u band' and (d) the C-d band. Here, 'u' and 'd' stand for "spin up" and "spin down", while positive and negative values are shown in red and blue, respectively. In (d), the atomic magnetic moments in the unit of μ_B (Bohr magneton) are also shown, with those of C atoms on the left side and those of Si atoms on the right side.

The transmission function of the junction with a parallel configuration (labelled as 'S1-P') is shown in Fig. 1(b). It is seen that the transmission at any energy is an integer. It is natural since all Bloch states can be transmitted without any scattering and each Bloch state will contribute 1 to the transmission when the potential is periodic. In this case, the band structures of the left and right leads are presented in Fig. 1(c) and (d), respectively. There is one to one correspondence for each energy-momentum (E–k) pair. Specifically, the transmission for each spin channel at around the Fermi level is exactly 1.0. The scattering states and the atom projected density of scattering states (DOSS) at the Fermi energy are shown in Fig. 3. The scattering states are the eigenstates of a two-probe device, demonstrating how a Bloch state incoming from one lead is transmitted and reflected when passing the scattering center. The scattering states shown in Fig. 3(a and b) indicate that the Bloch state does not decay after passing the central region. The DOSS at a specific energy reflects better the scattering process than the scattering states since it is the integration of the scattering state over the real space and projection onto each atom, while the scattering state shown in Fig. 3(a and b) only shows the information of the real part or the imaginary part at a specific isovalue. It is seen that the magnitude of the atomic projected DOSS (Fig. 3(c and d)) keeps fixed or periodic when going from left to right, indicating perfect transmission in this case.

However, for the anti-parallel configuration (labelled as 'S1-AP', see Fig. 4(a)), the spin indices of the bands in the right lead are exchanged, as compared with those of the left lead (see Fig. 4(c and d)). Now it is seen that the transmission around the Fermi level is exactly zero, suggesting the complete blocking of electrons (see Fig. 4(b)). The scattering states and the atomic projected DOSS shown in Fig. 5 also reflect the complete blocking of electrons. It is very strange and interesting, considering that none of the three factors above, namely, zero density of states, orbital symmetry mismatch and spin mismatch, explains this blocking since, obviously, on the one hand, both spin channels cross the Fermi level in both leads, thus the spin mismatch does not occur and the density of states for each spin channel is nonzero, and on the other hand, the states of these bands are all localized on one edge and thus they do not have definite orthogonal symmetries to cause blocking between them.

However, two possible mechanisms may still cause the blocking in the anti-parallel configuration. The first one is the inter-edge spatial separation between the initial states and final states during the tunneling process. Take the spin up channel as an example. Let's focus on the spin up band marked with a red dot in each lead (see Fig. 1(c, d) and 4(c, d)).

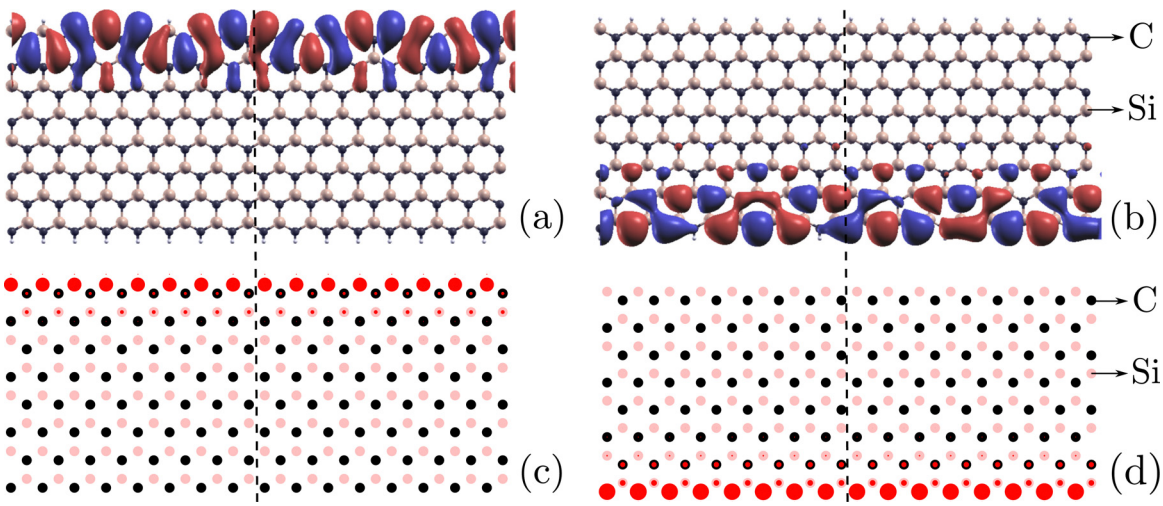

Fig. 3 The scattering state propagating from left to right at E = 0.0 eV in the S1-P case for (a) spin up and (b) spin down, with only the real (imaginary) part (not) shown since either of them reflects well the spatial distribution feature of the scattering state, and the density of scattering states (DOSS) for (c) spin up and (d) spin down. In (c) and (d), the black and pink balls indicate the positions of the C and Si atoms, while the size of the red filled circles shows the magnitude of the DOSS at the corresponding site. The central vertical dashed line marks the device central position along the transport direction.

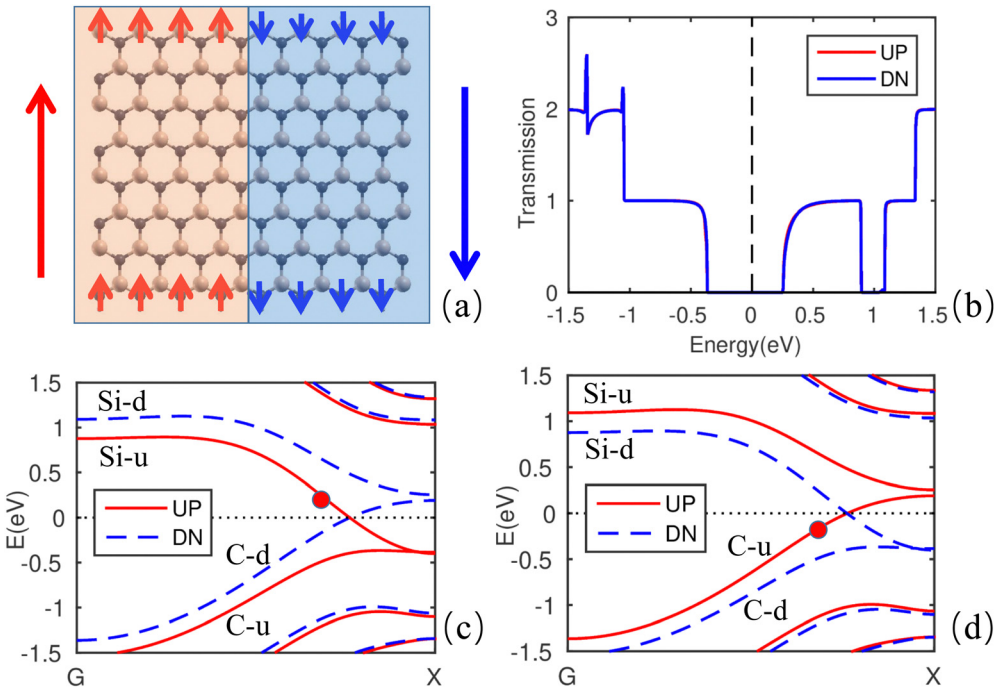

Fig. 4 (a) The central region of the device S1 with an anti-parallel magnetic configuration ("S1-AP"). (b) The equilibrium transmission function. (c) The band structure of the left lead. (d) The band structure of the right lead.

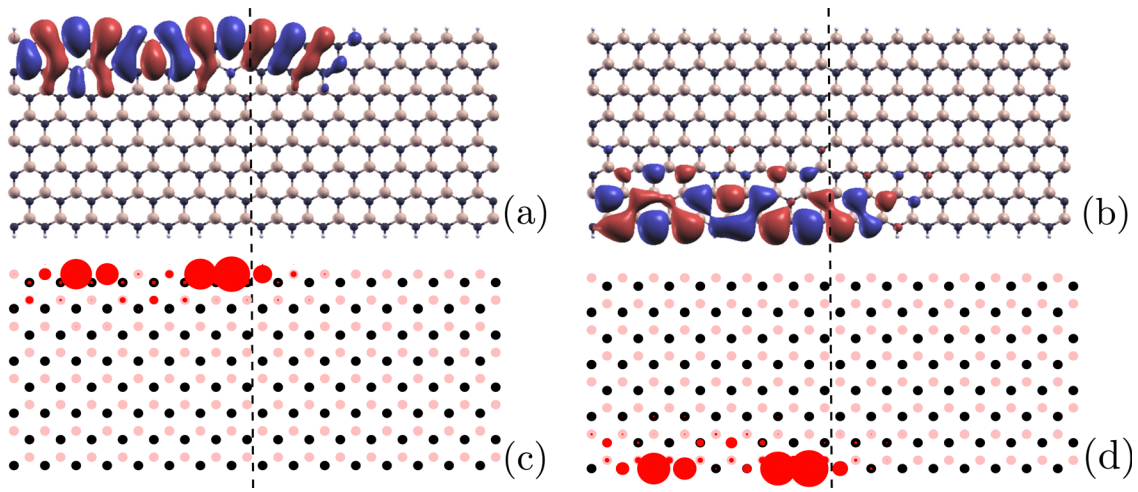

Fig. 5 The scattering state propagating from left to right at E = 0.0 eV in the S1-AP case for (a) spin up and (b) spin down, and the atom projected DOSS for (c) spin up and (d) spin down. In (c) and (d), the black and pink balls indicate the positions of the C and Si atoms, while the size of the red filled circles show the magnitude of the DOSS at the corresponding site.

The incoming state from the left lead is localized at the Si-edge, while the outgoing state is localized at the C-edge. There is an inter-edge spatial separation induced tunnel barrier between the upper edge (Si-edge) and the lower edge (C-edge). Shall this spatial separation induced barrier cause the complete blocking? The second one is the band dispersion of the two bands crossing the Fermi level in the two leads. It is seen that the slope of the Si-u band is negative while that of the C-u band is positive in the right half of the first Brillouin zone (see Fig. 3(c and d)). Will the different sign of the slope cause the complete blocking? To determine which one is the true factor that causes the blocking, we set up the following junction. We turn the right half of the central region and the right lead by π around the central axis along the transport direction and connect it to the left half of the central region. Now, the connection region is made up of Si–Si dimers and C–C dimers (see Fig. 6(a) and 8(a)). We still consider the parallel and anti-parallel magnetic configurations between the two leads and we will call these two configurations as 'S2-P' and 'S2-AP', respectively.

In 'S2-P', the band structure of the right lead is the same as that in the left lead since the magnetizations in both leads are pointing up. In this case, the spin up electrons will tunnel from the Si-u band in the left lead to the Si-u band in the right lead. However, the states in the Si-u band in the left lead and those in the right lead are localized at the upper edge and at the lower edge, respectively. Thus, the band slopes of the two bands between which the tunneling occurs are the same, but the spatial separation induced barrier will be developed between them. It is seen now that both spin channels are conducting well (see Fig. 6(b)), with the transmission at the Fermi level reaching about 0.5. The atomic projected DOSS in Fig. 7(a and b) also shows clearly the partial transmission of each spin channel and the transmission path switching from the top (bottom) edge to the bottom (top) edge for the spin up (down) channel. Thus, the inter-edge spatial separation induced tunnel barrier is not the cause for the electron transmission blocking.

In contrast, in 'S2-AP' (Fig. 8(a)), the two spin indices of the band structure in the right lead will be exchanged (Fig. 8(c and d)), just like that in 'S1-AP'. Now the states in the spin up channel in the left lead will be localized at the upper edge (Si-edge), and those in the right lead will also be localized at the upper edge (C-edge). In this case, there is no inter-edge spatial separation induced barrier between the initial state and the final state in the tunneling process. However, since the spin up state comes from the Si-u band in the left lead while it comes from the C-u band in the right lead, these two bands have opposite slope signs (see Fig. 8(c and d)). It is found that in this situation, the transmission of both spin channels around the Fermi level is extremely low (Fig. 8(b)). The atomic projected DOSS in Fig. 7(c and d) also shows that the two spin channels are blocked in this case. Thus, we may conclude that the blocking is caused by the slopes with opposite signs, not by the spatial separation induced tunnel barrier.

It is easy to understand since the slope actually determines the group velocity $v = \frac{1}{\hbar}\frac{\partial E}{\partial k}$. The transmission mode in the left lead and that in the right lead with the same k have opposite propagating directions; thus, it is impossible for a right moving wave in the left lead to continue to move right in a left moving mode in the right lead.[47] Although it is well known that the longitudinal k in the transport direction is not a good quantum number in a device and it may change in the tunneling process, it is believed that it can only change in a small range. According to the band symmetry, in the other half of the first Brillouin zone of the right lead, there are necessarily k points that have the same group velocity direction as the left lead. However, since the difference between the two k points that have matching group velocity is too large, the transmission between them will be small or even negligible. In the first Brillouin zone, half k points with a positive slope are responsible for electrons' right propagation while the other half points with a negative slope are responsible for electrons' left propagation. For electrons incoming from the left lead to continue to propagate in the right lead after passing the central region, the k points in the same half of the first Brillouin zone should have the same group velocity direction, which we call the momentum matching. In certain cases, the transmission may be nonzero even if the group velocity directions in the same moiety of the first Brillouin zones of the two leads are opposite. Such transmission occurs between two k points with the same group velocity direction from the different moieties of the first Brillouin zones

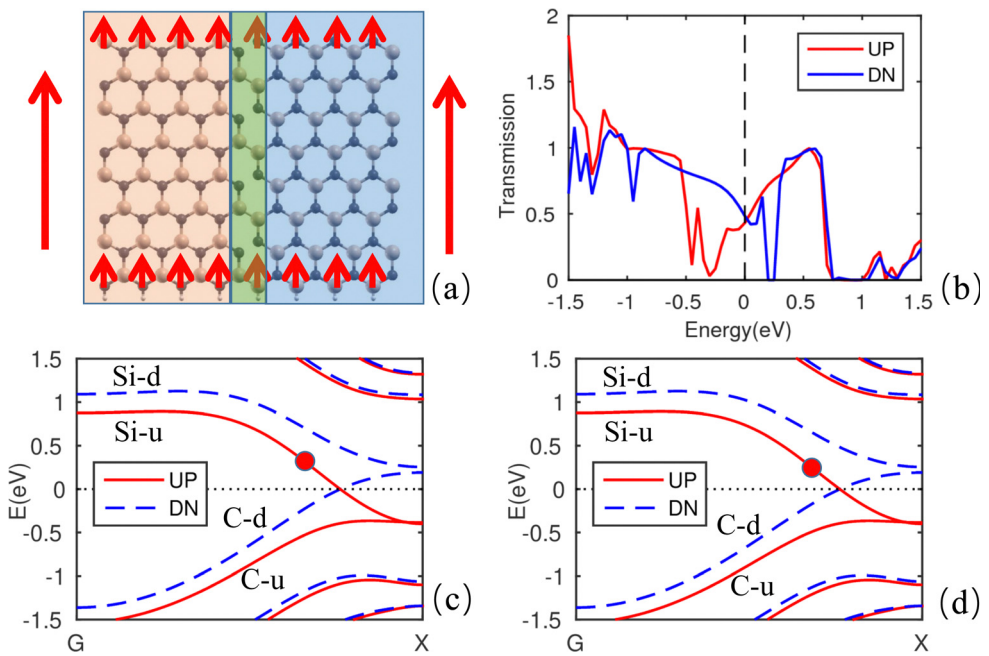

Fig. 6 (a) The central region of the device S2 with the parallel magnetic configuration ("S2-P"). (b) The equilibrium transmission function. (c) The band structure of the left lead. (d) The band structure of the right lead. The green box in (a) marks the connection region of the junction.

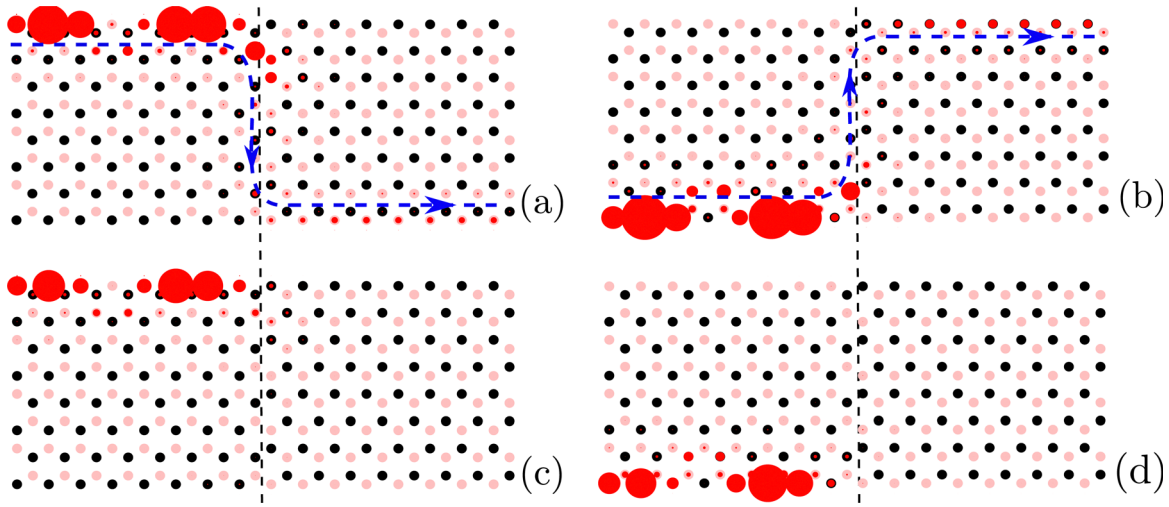

Fig. 7 The DOSS for the scattering state propagating from left to right at E = 0.0 eV in the S2-P case for (a) spin up and (b) spin down and that in the S2-AP case for (c) spin up and (d) spin down. The black and pink balls indicate the positions of the C and Si atoms, while the size of the red filled circles show the magnitude of the DOSS at the corresponding site. The blue dashed curves with arrows indicate transmission paths in the S2-P case.

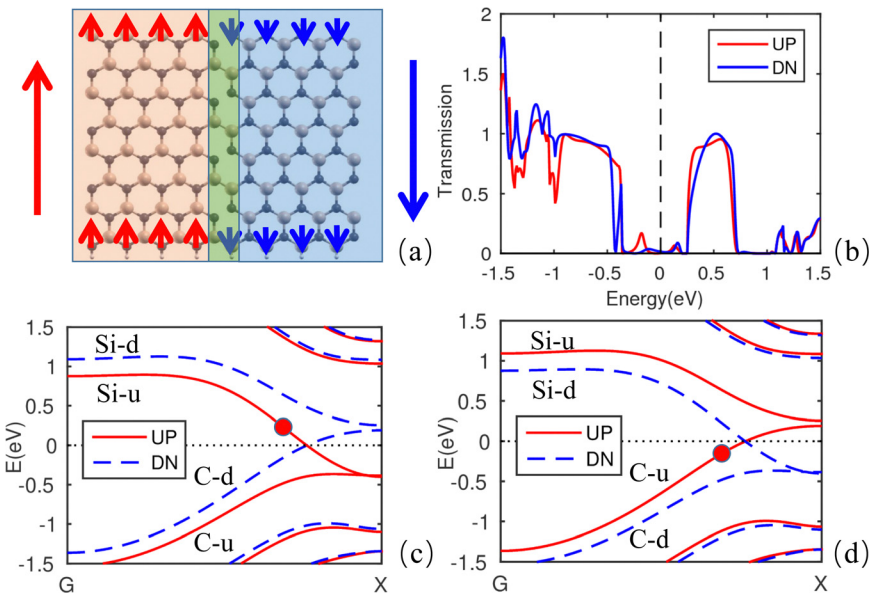

Fig. 8 (a) The central region of the device S2 with the anti-parallel magnetic configuration ("S2-AP"). (b) The equilibrium transmission function. (c) The band structure of the left lead. (d) The band structure of the right lead. The green box in (a) marks the connection region of the junction.

of the two leads. Although nonzero, it will be much smaller than the cases with the same group velocity in the same moiety of the first Brillouin zone due to the large k difference. The large k difference in the two leads is not beneficial for electron transport, which is particularly important in valleytronics where inter-valley scatterings are generally negligible just for this reason. Consequently, the momentum matching effect serves as a basic mechanism for designing electrical switching devices or GMR devices. To check the feasibility and the robustness of this mechanism, we have performed calculations on SiC nanoribbon junctions with different ribbon widths and the conductor–insulator transition together with the reversal of the magnetic configurations has always been achieved.

4. Conclusions

In summary, we have studied the spin polarized transport in a magnetic tunnel junction constructed with a ferromagnetic 8-ZSiCNR using density functional calculations. By switching the magnetization direction of the right lead, a metal-to-insulator transition behavior is observed, namely, two conducting and

insulating states are achieved, which definitely leads to giant magnetoresistance. The insulating state is not caused by any present formalisms, such as zero DOS, orbital symmetry mismatching or spin mismatching, but by a new formalism that we call momentum mismatching. This suggests a fantastic scheme for designing giant magnetoresistance by only considering or manipulating the matching or mismatching of the band dispersion of the materials. Although the device is actually a continuous nanoribbon in this work, the momentum mismatching effect can be extended to other systems that have two leads with opposite group velocity directions.

Author contributions

X. H. Zheng proposed the initial idea. Y. H. Qiu performed the calculations. All authors discussed the results and contributed to the preparation of the manuscript.

Conflicts of interest

There are no conflicts of interest to declare.

Acknowledgements

We gratefully acknowledge the support from the National Natural Science Foundation of China (grant no. 11974355, 61974068,12074230 and 12274111), the National Key R & D Program of China (grant no. 2022YFA1404003), the Shanxi Province 100-Plan Talent Program and the Fund for Shanxi "1331 Project".

Notes and references

1 G. Binasch, P. Grünberg, F. Saurenbach and W. Zinn, *Phys. Rev. B: Condens. Matter Mater. Phys.*, 1989, **39**, 4828–4830.
2 M. N. Baibich, J. M. Broto, A. Fert, F. N. Van Dau, F. Petroff, P. Etienne, G. Creuzet, A. Friederich and J. Chazelas, *Phys. Rev. Lett.*, 1988, **61**, 2472–2475.
3 I. Z. Žutic, J. Fabian and S. Das Sarma, *Rev. Mod. Phys.*, 2004, **76**, 323–410.
4 F. Pulizzi, *Nat. Mater.*, 2012, **11**, 367.
5 J.-J. He, F.-W. Guo, H.-M. Ni, J.-R. Yuan, W.-D. Cui, T.-Y. Lu, Y.-D. Guo and X.-H. Yan, *Phys. Chem. Chem. Phys.*, 2022, **24**, 25656–25662.
6 H.-M. Ni, J.-J. He, F.-W. Guo, J.-B. Dong, T.-Y. Lu, W.-D. Cui, J.-R. Yuan, Y.-D. Guo and X.-H. Yan, *Phys. Chem. Chem. Phys.*, 2023, **25**, 2342–2348.
7 A. Fert, *Rev. Mod. Phys.*, 2008, **80**, 1517–1530.
8 Y. An, Y. Hou, K. Wang, S. Gong, C. Ma, C. Zhao, T. Wang, Z. Jiao, H. Wang and R. Wu, *Adv. Funct. Mater.*, 2020, **30**, 2002939.
9 Y. Gao, J. Liao, H. Wang, Y. Wu, Y. Li, K. Wang, C. Ma, S. Gong, T. Wang, X. Dong, Z. Jiao and Y. An, *Phys. Rev. Appl.*, 2022, **18**, 034033.
10 J.-J. He, F.-W. Guo, H.-M. Ni, J.-B. Dong, W.-D. Cui, T.-Y. Lu, J.-R. Yuan, Y.-D. Guo and X.-H. Yan, *J. Chem. Phys.*, 2023, **158**, 204105.
11 Y. An, K. Wang, S. Gong, Y. Hou, C. Ma, M. Zhu, C. Zhao, T. Wang, S. Ma, H. Wang, R. Wu and W. Liu, *npj Comput. Mater.*, 2021, **7**, 45.
12 J.-J. He, H.-M. Ni, F.-W. Guo, J.-B. Dong, W.-D. Cui, T.-Y. Lu, J.-R. Yuan, Y.-D. Guo and X.-H. Yan, *J. Alloys Compd.*, 2023, **961**, 170989.
13 S. Yuasa, T. Nagahama, A. Fukushima, Y. Suzuki and K. Ando, *Nat. Mater.*, 2004, **3**, 868–871.
14 K. S. Novoselov, A. K. Geim, S. V. Morozov, D. Jiang, Y. Zhang, S. V. Dubonos, I. V. Grigorieva and A. A. Firsov, 2004.
15 H. Su, T. Hu, F. Wu and E. Kan, *J. Phys. Chem. C*, 2021, **125**, 10738–10746.
16 D. Chen, Z. Jiang, Y. Tang, J. Zhou, Y. Gu, J.-J. He and J. Yuan, *Front. Chem.*, 2022, 10.
17 Z. Zhang, T. Shi, J. He, C. Liu, L. Meng and X. Yan, *Semicond. Sci. Technol.*, 2023, **38**, 045009.
18 Y. Zheng, Y. Wang, Z. Wang, X. Li, Y. Liang, C. Huang and F. Wu, *J. Phys. Chem. C*, 2022, **126**, 17390–17397.
19 L. Ji, Y. Wang, Y. Zheng, Z. Wang, J. Wang, Y. Liu and F. Wu, *J. Phys. Chem. C*, 2021, **125**, 15664–15669.
20 C. Gong, L. Li, Z. Li, H. Ji, A. Stern, Y. Xia, T. Cao, W. Bao, C. Wang and Y. Wang, *Nature*, 2017, **546**, 265.
21 B. Huang, G. Clark, E. Navarro-Moratalla, D. R. Klein, R. Cheng, K. L. Seyler, D. Zhong, E. Schmidgall, M. A. McGuire, D. H. Cobden, W. Yao, D. Xiao, P. Jarillo-Herrero and X. Xu, *Nature*, 2017, **546**, 270–273.
22 M. Bonilla, S. Kolekar, Y. Ma, H. C. Diaz, V. Kalappattil, R. Das, T. Eggers, H. R. Gutierrez, M.-H. Phan and M. Batzill, *Nat. Nanotechnol.*, 2018, **13**, 289–293.
23 C. Gong, L. Li, Z. Li, H. Ji, A. Stern, Y. Xia, T. Cao, W. Bao, C. Wang and Y. Wang, *et al.*, *Nature*, 2017, **546**, 265–269.
24 Y. Deng, Y. Yu, Y. Song, J. Zhang, N. Z. Wang, Z. Sun, Y. Yi, Y. Z. Wu, S. Wu and J. Zhu, *et al.*, *Nature*, 2018, **563**, 94–99.
25 N. Miao, B. Xu, L. Zhu, Z. Jian and Z. Sun, *J. Am. Chem. Soc.*, 2018, **140**, 2417–2420.
26 Q. Wu, Y. Zhang, Q. Zhou, J. Wang and X. C. Zeng, *J. Phys. Chem. Lett.*, 2018, **9**, 4260–4266.
27 C. Huang, Y. Du, H. Wu, H. Xiang, K. Deng and E. Kan, *Phys. Rev. Lett.*, 2018, **120**, 147601.
28 A. H. Castro Neto, F. Guinea, N. M. R. Peres, K. S. Novoselov and A. K. Geim, *Rev. Mod. Phys.*, 2009, **81**, 109–162.
29 S. Chabi, Z. Guler, A. J. Brearley, A. D. Benavidez and T. S. Luk, *Nanomaterials*, 2021, **11**, 1799.
30 F. Muñoz-Rojas, J. Fernández-Rossier and J. J. Palacios, *Phys. Rev. Lett.*, 2009, **102**, 136810.
31 Z. Han, H. Hao, X. Zheng and Z. Zeng, *Phys. Chem. Chem. Phys.*, 2023, **25**, 6461–6466.
32 W. Y. Kim and K. S. Kim, *Nat. Nanotechnol.*, 2008, **3**, 408–412.
33 J. Bai, R. Cheng, F. Xiu, L. Liao, M. Wang, A. Shailos, K. L. Wang, Y. Huang and X. Duan, *Nat. Nanotechnol.*, 2010, **5**, 655–659.

34 K. Gopinadhan, Y. J. Shin, R. Jalil, T. Venkatesan, A. K. Geim, A. H. C. Neto and H. Yang, *Nat. Commun.*, 2015, **6**, 8337.
35 Y.-T. Zhang, H. Jiang, Q.-F. Sun and X. C. Xie, *Phys. Rev. B: Condens. Matter Mater. Phys.*, 2010, **81**, 165404.
36 P. Jiang, L. Kang, H. Hao, X. Zheng, Z. Zeng and S. Sanvito, *Phys. Rev. B*, 2020, **102**, 245417.
37 X. H. Zheng, J. Lan, X. L. Wang, L. F. Huang, H. Hao and Z. Zeng, *Appl. Phys. Lett.*, 2012, **101**, 053101.
38 J. Maassen, M. Harb, V. Michaud-Rioux, Y. Zhu and H. Guo, *Proc. IEEE*, 2012, **101**, 518–530.
39 J. Taylor, H. Guo and J. Wang, *Phys. Rev. B: Condens. Matter Mater. Phys.*, 2001, **63**, 245407.
40 J. P. Perdew, K. Burke and M. Ernzerhof, *Phys. Rev. Lett.*, 1996, **77**, 3865.
41 Z. Afshoon and T. Movlarooy, *Silicon*, 2023, **15**, 4149–4158.
42 A. Mulatu, K. Nigussa and L. Deja, *Materialia*, 2021, **20**, 101257.
43 H. Zhang, W. Ding, K. He and M. Li, *Nanoscale Res. Lett.*, 2010, **5**, 1264–1271.
44 P. Lou and J. Y. Lee, *J. Phys. Chem. C*, 2009, **113**, 12637–12640.
45 C. D. Costa and J. M. Morbec, *J. Phys.: Condens. Matter*, 2011, **23**, 205504.
46 Y. Ding and Y. Wang, *Appl. Phys. Lett.*, 2012, **101**, 013102.
47 X. Zheng, X. Chen, L. Zhang, L. Xiao, S. Jia, Z. Zeng and H. Guo, *2D Mater.*, 2017, **4**, 025013.

